Soft Matter

PAPER

View Article Online
View Journal | View Issue

Cite this: *Soft Matter*, 2021, **17**, 947

Temperature-induced liquid crystal microdroplet formation in a partially miscible liquid mixture†

Mehzabin Patel, [a] Anand N. P. Radhakrishnan, [a] Ludovic Bescher, [ab] Elwin Hunter-Sellars, [a] Benjamin Schmidt-Hansberg, [c] Esther Amstad, [b] Stuart Ibsen [ad] and Stefan Guldin *[a]

Received 29th September 2020,
Accepted 9th November 2020

DOI: 10.1039/d0sm01742f

rsc.li/soft-matter-journal

Liquid-in-liquid droplets are typically generated by the partitioning of immiscible fluids, *e.g.* by mechanical shearing with macroscopic homogenisers or microfluidic flow focussing. In contrast, partially miscible liquids with a critical solution temperature display a temperature-dependent mixing behaviour. In this work, we demonstrate how, for a blend of methanol (MeOH) and the thermotropic liquid crystal (LC) 4-Cyano-4′-pentylbiphenyl (5CB), cooling from a miscible to an immiscible state allows the controlled formation of microdroplets. A near-room-temperature-induced phase separation leads to nucleation, growth and coalescence of mesogen-rich droplets. The size and number of the droplets is tunable on the microscopic scale by variation of temperature quench depth and cooling rate. Further cooling induces a phase transition to nematic droplets with radial configuration, well-defined sizes and stability over the course of an hour. This temperature-induced approach offers a scalable and reversible alternative to droplet formation with relevance in diagnostics, optoelectronics, materials templating and extraction processes.

Introduction

The nucleation and growth of microscopic droplets is of profound and widespread relevance in colloidal and interfacial science and technology.[1,2] Regular binary liquid mixtures exhibit a miscibility gap for certain compositions and temperature ranges. For a mixture with an upper critical solution temperature (UCST), the system is monophasic above the temperature threshold. Cooling below the coexistence curve in the corresponding phase diagram of temperature T and composition ϕ induces either spontaneous phase separation by spinodal decomposition or a metastable state, where phase separation occurs by nucleation and growth.[3]

The intrinsic, spontaneous formation and growth of nuclei upon cooling of binary fluid systems has been studied from a theoretical perspective of the phase ordering process.[4–8] Much work has been done to understand systems showing condensation,[9] crystallisation,[10] phase separation of binary alloys,[11] and more recently liquid crystal mixtures.[12–14] The growth of a nucleus or a droplet typically obeys a universal growth law, which follows the growth of a characteristic length (L), and is usually defined by the diameter of the nuclei.

$$L(t) \sim t^n, \tag{1}$$

with t as the time after a temperature quench to induce phase transition or separation and n as the universal growth exponent.[6] For material systems with conserved order parameters, such as the phase separation of binary blends, a growth exponent of 1/3 is predicted.[15,16] For material systems with non-conserved order parameters, such as liquid crystals, the growth exponent is expected to depend on the temperature quench depth, varying from 1/2 to 1.[6,12,17] This behaviour has been primarily investigated in material systems pertaining to isotropic fluids.[8,18–22] In addition, studies have been performed on binary mixtures of two liquid crystals with distinct transition temperatures,[23] isotropic liquids with the liquid crystal as the continuous phase,[24,25] and droplets of liquid crystals in a polymer matrix (PDLC).[26,27] To the best of our knowledge, the formation of liquid crystal microdroplets in an isotropic non-polymeric continuous phase by temperature-induced phase separation has not been studied.

The confinement of liquid crystals (LCs) in microdroplet form offers an intriguing combination of control over the composition and microscopic structure, including well-defined mesogen orientations, enhanced interfacial area, a rich phase space, tunable optical properties and stimuli response.[28–35] LC microdroplets

[a] *Department of Chemical Engineering, University College London, Torrington Place, London, WC1E 7JE, UK. E-mail: s.guldin@ucl.ac.uk*
[b] *Institute of Materials, École Polytechnique Fédérale de Lausanne (EPFL), Station 12, 1015 Lausanne, Switzerland*
[c] *BASF SE, Process Research & Chemical Engineering, Coating & Film Processing, Carl-Bosch-Strasse 38, 67056 Ludwigshafen am Rhein, Germany*
[d] *School of Medicine, Oregon State and Science University, Portland, OR 97239, USA*

† Electronic supplementary information (ESI) available. See DOI: 10.1039/d0sm01742f

embedded in a polymer matrix have attracted considerable interest in optoelectronic applications, such as variable transmittance windows and reflective mode displays.[27,36,37] Solution-dispersed LC droplets are a promising platform for chemo- & biosensing.[38,39] Typically, sensing is driven by the ability to optically read-out target recognition-driven ordering transitions. This has been successfully demonstrated for a range of analytes, such as bacteria and viruses (10^4 pfu mL^{-1}),[40] endotoxin (pM),[41] protein immunoassays (pM),[39] and lithocholic acid (μM).[42] Other applications include the use of LC microdroplets as self-reporting and self-regulating containment for controlled cargo release,[43] tunable optical microresonators,[44–47] microlasers,[48,49] optical switches,[50,51] light responsive 3D superstructures,[52] microswimmers,[53–55] as well as for materials templating.[56]

Here, we study how a partially miscible liquid–liquid crystal mixture enables the temperature-induced formation of liquid crystal microdroplets. We investigate the droplet evolution to resolve nucleation and growth processes and identify critical parameters that govern the number and size distribution of LC droplets. Finally, we quench the liquid mixture below the isotropic-to-nematic transition temperature and study the feasibility of this approach for the generation of temperature-stable and well-defined nematic droplets.

Experimental section

Reagents

The liquid crystal 4-Cyano-4′-pentylbiphenyl (5CB) was obtained from Synthon Chemicals (99.5% (GC)). MeOH (HPLC grade) was purchased from Sigma Aldrich. All compounds were used without further purification.

Sample preparation

Samples of 5CB:MeOH were mixed in a glass cuvette, which was enclosed by a Peltier-regulated sample compartment that allowed control over both temperature and stirring (Quantum Northwest, Qpod 2e). Unless stated otherwise, a 30 : 70 volume ratio of 5CB:MeOH was used for all experiments. Samples were heated to 35 °C in the cuvette. Glass slides were functionalised to increase the hydrophobicity of the surface. First, an oxygen plasma etcher was used to clean the surface and increase wettability of the slides. The glass slides were then placed in a bath of 0.1 mM solution of trichloro(octyl)silane (97%, purchased from Sigma Aldrich) in heptane (≥ 99.9%, purchased from Sigma Aldrich) for 10 minutes. Finally, they were washed in MeOH (HPLC grade). For microscopic analysis, 10 μl of the homogeneous mixture was deposited between a functionalised glass slide and cover slip and sealed with varnish (purchased from Rimmel: 15–40% ethyl acetate, 15–40% butyl acetate, 5–15% nitrocellulose, 1–10% isopropylalcohol) to prevent MeOH evaporation.

Sample analysis

The slide was placed under an upright microscope (Zeiss, Axio Scope A1), that was operated in transmission and primarily in brightfield mode. A temperature controlled sample stage (Linkam, PE120) was used for all experiments. For low temperature experiments, nitrogen was introduced into the chamber to prevent condensation. *In situ* droplet formation and short-term growth were recorded by time-resolved digital image acquisition using a Photron Fastcam MC1 high-speed camera taking 50 frames per second (fps) at a resolution of 512 × 512 pixels. For nematic droplet analysis, a Lumenera Infinity 3-3UR camera was used, taking 1 fps with a resolution of 1936 × 1456 pixels. For temperature quench and cooling rate experiments, the cell was heated to 35 °C and then cooled at a defined cooling rate ranging between 1 °C min^{-1} and 20 °C min^{-1} to a target temperature below the critical temperature, T_c. Note that for the purpose of this study, T_c is referred to as the temperature at which phase separation occurs and the quench depth ΔT relates to $|T_{target} - T_c|$. With a 30 : 70 vol% mixture of 5CB : MeOH, the T_c was 22.5 °C. Quantitative droplet investigation was carried out by a bespoke computational image analysis code developed in Python [full details can be found in the ESI†]. The fully automated analysis protocol enabled the extraction of otherwise unattainable kinetic information. Droplets from the high-speed images were identified, distinguished, and the number of droplets, the average diameter as well as standard deviation computed as a function of time.[57] Calculation of trajectories, displacement and MSD of droplets was carried out using Fiji. Droplets were tracked using the Particle Detector and Tracker plugin: MOSAIC,[58] which outputs the x and y coordinates of each trajectory for further calculation.

Results and discussion

We have recently reported on the macroscopic phase behaviour of a binary mixture composed of the thermotropic nematic liquid crystal 4-Cyano-4′pentylbiphenyl (5CB) and methanol (MeOH).[59] Four different arrangements were found as a function of temperature and volume fraction, namely monophasic isotropic, monophasic nematic, biphasic isotropic-isotropic and biphasic isotropic-nematic. This system displays a $T-\phi$ phase diagram with an UCST of 25 °C. According to Gibbs, a spinodal curve divides the region inside the phase coexistence curve of a phase diagram into an unstable region, in which phase separation is driven by spinodal decomposition, and a metastable region where phase separation is triggered through a nucleation and growth process.[5] Droplets that form by temperature-induced phase separation nucleate when reaching a critical size to overcome the energy barrier associated with forming a new interface.[5] For an off-critical mixture as used herein, demixing typically occurs *via* nucleation and growth. The phase behaviour was subsequently implemented in thermo-responsive microfluidic architectures[60] and further investigated for binary mixtures of 5CB and ethanol.[61]

Microdroplet formation was studied by optical microscopy in a 18 × 18 mm^2 sealed sample compartment of 30 μm thickness. A binary liquid mixture of 30 vol% 5CB, 70 vol% MeOH was used for all experiments, unless stated otherwise.

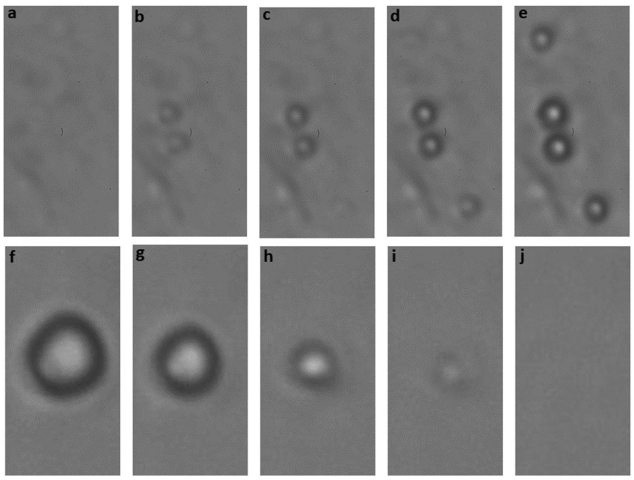

Fig. 1 Reversible droplet formation. (a)–(e) Nucleation and early-stage growth of isotropic droplets over the initial 0.2 s at 22.5 °C. (f)–(j) Disappearance of mature droplets over 7 s upon heating to 35 °C. Image width: 10 μm.

Fine temperature control was achieved by an enclosed Peltier-driven sample stage. A characteristic example for the nucleation and growth process observed under high speed imaging is shown in Fig. 1a–e. Samples were heated to 35 °C, a temperature well above their critical solution temperature, to ensure a monophasic solution. When cooled from 35 °C at a rate of 1 °C min^{-1}, droplets began to nucleate at 22.5 °C and grow. The nucleation of these droplets occurred over 0.2 s. If adjacent droplets met, they coalesced. These droplets were allowed to grow and mature. Upon reheating of the sample up to 35 °C at 1 °C min^{-1}, the droplets disappeared and became monophasic, as shown in the sequence of images in Fig. 1f–j. The temperature where microdroplets formed is in good agreement with the macroscopic critical solution temperature for a mixture of 30 vol% 5CB and 70 vol% MeOH recently reported by our group.[59]

5CB/MeOH temperature quench

Droplet growth upon demixing for off-critical mixtures of binary fluids is generally described in three phases. Nucleation occurs when a concentration partitioning reaches a critical size (phase I, timescale: μs), after which the droplet will grow spontaneously by diffusion (phase II, timescale: ms). Thereafter or simultaneously, the droplets undergo further growth by coalescence and Ostwald ripening (phase III, timescale: s–min).[8,62,63] Eventually, the decreasing motion of droplets and increasing interdroplet spacing leads to a significant reduction in the rate of droplet growth and the system reaches an interim or steady state (>30 s).

Fig. 2a–c displays microscopic images of 5CB-rich droplets in MeOH 20 s after nucleation with quench depths (ΔT) of 0.5 °C (a), 2.5 °C (b) and 7.5 °C (c), respectively. The quench depth relates to the undercooling with respect to the critical solution temperature (T_c), with $\Delta T = |T_{target} - T_c|$. Images were acquired at frame rates of 50 images per second and analysed using a custom-built and fully automated computational approach as detailed in the ESI† (Fig. SI1 and SI2). Fig. 2d depicts a time-resolved evolution of the mean droplet size for different quench depths. While a shallow quench depth of 0.5 °C led to a droplet diameter of around 4.7 ± 1.2 μm at 60 s, a quench depth of 2.5 °C resulted in droplets of 7.6 ± 2.2 μm in size, increasing ΔT to 7.5 °C caused a further increase in droplet diameter to 10.4 ± 2.2 μm within the observed time span as shown in Fig. 2d. Following eqn (1), increasing the quench depth (ΔT) from 0.5 °C to 2.5 °C and 7.5 °C led to an increasing growth exponent of 0.19, 0.32 and 0.35, respectively, in the first stages of droplet growth. The dependence of the growth exponent on quench depth is in agreement with previous studies.[12,23] However, this was primarily discussed for phase transitions, where the growth exponent increased from 0.5 to 1, rather than phase separations. For phase transitions, the dependence of the growth exponent on quench depth was related to a larger difference in free energy between the isotropic and the ordered state.[6,12]

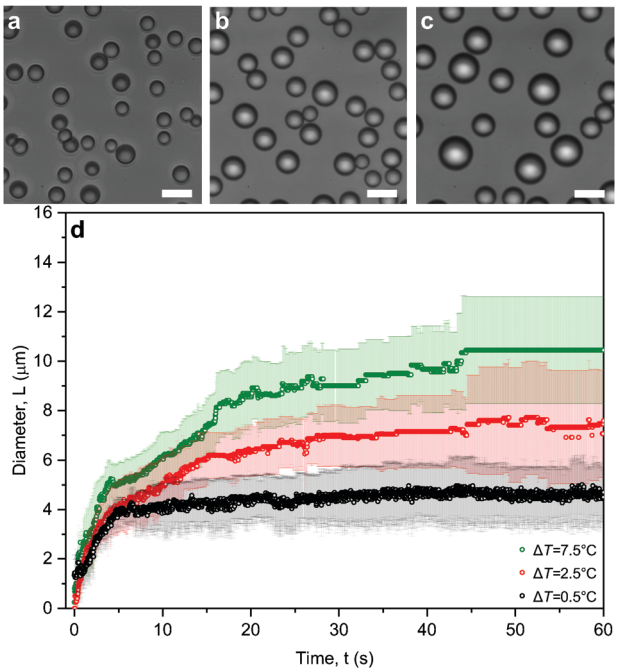

Fig. 2 Droplet diameter *vs.* quench depth. (a)–(c) Microscopic images of isotropic 5CB-rich droplets in MeOH 20 s after nucleation at quench depths of (a) 0.5 °C, (b) 2.5 °C and (c) 7.5 °C. In all cases, the mixture was cooled from 35 °C at a cooling rate of 20 °C min^{-1}. The scale bar represents 10 μm. (d) Overview of droplet mean diameter and standard deviation for respective quench depths over time.

Notably, the dependence of the mean droplet size once reaching ready state on the temperature quench ΔT is in line with a study by Luo and coworkers for supersaturation-induced emulsions, who found that the droplet volume was linearly proportional to the applied quench depth.[63] In our work, the observed droplet diameter of 4.7 ± 1.2 μm (ΔT = 0.5 °C), 7.6 ± 2.2 μm (ΔT = 2.5 °C) and 10.4 ± 2.2 μm (ΔT = 7.5 °C) also followed closely a $R \propto \Delta T^{1/3}$ relationship.

Analysis of the number of droplets as a function of time (ESI,† Fig. SI3) provided further insights. For a quench depth of

0.5 °C, the number of droplets increased over 20 s and then settled slightly below the maximum level. In contrast, at ΔT = 7.5 °C droplets appeared within the first seconds and then reduced in count significantly over time. Previous research focussed on the effect of quench depth on the critical nucleus size, with an understanding that with increasing quench depth, the free energy barrier to nucleation decreases to values similar to the energy of thermal fluctuations at the spinodal.[4,64] In this context, the critical nucleus size was found to decrease with an increasing quench depth,[64] which is in line with our observations.

The dispersity of droplets was further investigated by analysis of larger sample sizes, using images acquired at frame rates of 1 image per second. The droplet population is presented in a histogram in Fig. 3a–c over the course of the initial 60 s. Notably, the evolution of both droplet size and size distribution was found to depend strongly on the quench depth (ΔT). For Δ0.5 °C (a), the droplets remained relatively stable, with some larger droplets that formed at the expense of smaller ones. In contrast, for Δ7.5 °C (c), the droplet population became multimodal after 30 s, with an overall profound size increase and broadening of the detected droplet diameters. Droplet motion was analysed through individual trajectories along the x and y axis, as presented in Fig. 3d–f. Each droplet was followed throughout its residence in the field of view. The colour coding in the legend illustrates the time t_0 when the droplet first entered the frame, *i.e.* for t_0 = 0 s the droplets formed within the field of view, while for $t_0 \geq 0$ s the droplets formed elsewhere, then moved inside the field of view and were tracked thereafter. For a quench depth of 0.5 °C (d), the motion was essentially random around the starting position, with few droplets exhibiting directional motion away from the starting point.

As the quench depth increased to 2.5 °C (e), there were more instances of directional motion with some random fluctuation around the starting position. At a quench depth of 7.5 °C (f), droplet movement appeared primarily directional and along the same axis. Hence, in addition to diffusion and coalescence led by Brownian motion, we identified a directional motion of the droplets, which became more pronounced with increasing quench depth. The corresponding mean square displacement (MSD) is shown in Fig. 3g–i as a function of time lag, τ, with $\tau = t - t_0$. If the droplet trajectories were solely led by diffusion, a linear correlation between the quench depth and the MSD would be expected. However, the curvature of the graphs, particularly at large quench depths, suggests an external force. In comparison to the steep increase in MSD for $t_0 < 10$ s, a shallow incline was observed for droplets that moved later into the field of view, suggesting that the directional droplet motion was a direct consequence of the applied cooling and faded thereafter. A likely cause of directional droplet motion in immiscible fluid mixtures is related to Marangoni-driven flow, where a temperature gradient across the droplet interface leads to non-uniformity in surface tension. This was demonstrated in detail by Karbalaei *et al.*[79] In our experimental set up, droplets were formed in a liquid cell that was cooled on a microscopy temperature stage with circular cut-out. As a consequence, cooling resulted in a temperature gradient from edge to centre. We found the droplets to be driven from the hot to the cold region, *i.e.* from vicinity to centre. As the quench depth (ΔT) was increased, a larger temperature gradient was observed along the plate for a longer period of time, thus increasing directional droplet motion.

Our findings emphasise the factors that influence droplet growth by coalescence, namely the interdroplet distance and

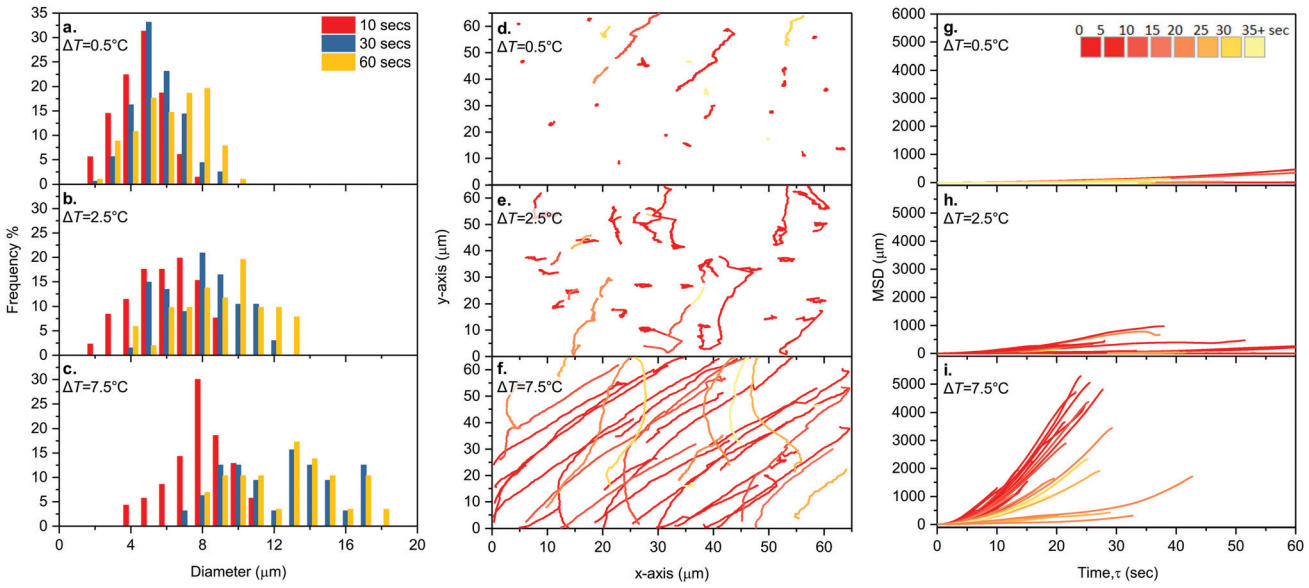

Fig. 3 Dispersity and trajectory of droplets (a)–(c) Diameter histogram of isotropic 5CB droplets over time at quench depths of (a) Δ0.5 °C, (b) Δ2.5 °C, (c) Δ7.5 °C. (d)–(f) Trajectory of droplets along the x and y axis over the course of 60 seconds at quench depths of (d) 0.5 °C, (e) 2.5 °C, (f) 7.5 °C. (g)–(i) Mean square displacement of droplets at quench depths of (g) 0.5 °C, (h) 2.5 °C, (i) 7.5 °C over time. The colour coding relates to the time at which a new droplet entered the frame.

the droplet motion, both of which are affected by the temperature quench. Eventually, with increased spacing and reduced mobility, the droplets reached a steady state, after which only rare events of further coalescence and Ostwald ripening were observed.

5CB/MeOH cooling rate

We further investigated the effect of cooling rate on droplet formation and growth, as shown in Fig. 4. In all experiments, a homogeneous mixture of 5CB and MeOH was cooled from 35 °C to 15 °C, with a quench depth of 7.5 °C below T_c at cooling rates varying between 20 °C min^{-1} and 1 °C min^{-1}. For all cooling rates, a representative snapshot of LC droplets taken 5 s after nucleation, is shown in Fig. 4a–d. Results from the automated computational analysis of droplets are presented in Fig. 4e.

Cooling rates of 20 °C min^{-1} led to greatly increased initial numbers of droplets, which rapidly decayed over the first 20 s. In contrast, slower cooling rates resulted in a lower initial number of droplets which remained more constant over time. The development of the number of droplets with time may be directly related to the droplet density. Faster cooling rates ($\geq$10 °C min^{-1}) led to a higher droplet density and thus smaller interdroplet distances, which in turn implied a higher probability for coalescence. We note that at a cooling rate of 1 °C min^{-1}, the number of nucleated droplets was ten times less in comparison to a cooling rate of 20 °C min^{-1}. The rate of cooling and related droplet density had a direct impact on the observed growth mode; at high cooling rates, droplet growth was dominated by coalescence. In contrast, at lower cooling rates and enhanced interdroplet distances, the growth was predominantly driven by diffusion. As a result, the cooling rate affected the polydispersity for droplet diameter: slow cooling rates of 1 °C min^{-1} resulted in a smaller average diameter and standard deviation compared to fast cooling rates of 20 °C min^{-1}. To quantify the droplet movement, we analysed the individual droplet trajectories as detailed in the ESI† (Fig. SI4). While we observed directional motion for both 1 °C min^{-1} and 20 °C min^{-1}, the gradient of the MSD was cooling rate dependent. As pointed out above, faster cooling rates and thus higher droplet densities implied a higher probability for coalescence. Thus, the increased MSD may be a direct consequence of coalescence-induced coalescence cascade processes and related hydrodynamic flow.[65–67]

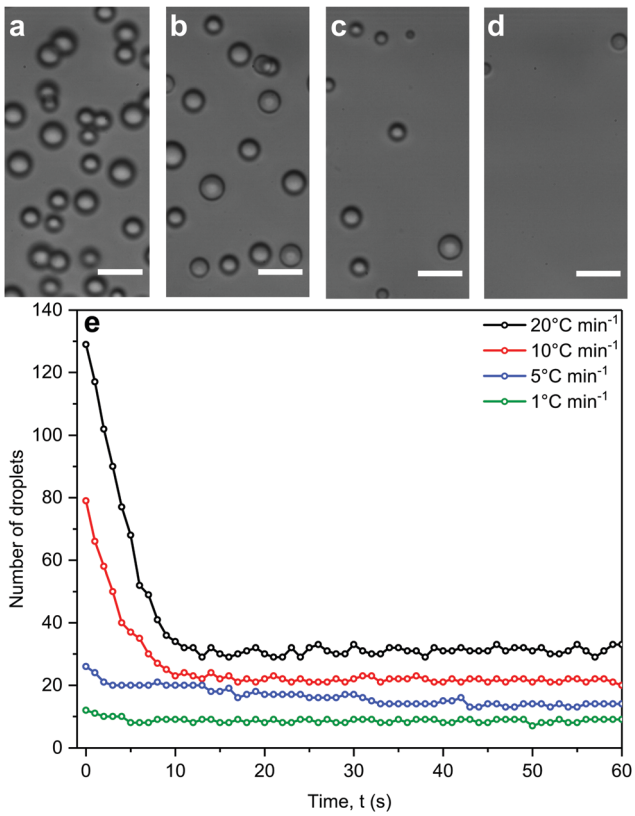

Fig. 4 Droplet number *vs.* cooling rate. (a)–(d) Microscopic images of isotropic 5CB droplets in MeOH 5 s after nucleation at cooling rates of (a) 20 °C min^{-1}, (b) 10 °C min^{-1}, (c) 5 °C min^{-1} and (d) 1 °C min^{-1} for a quench depth of 7.5 °C. The scale bar represents 10 μm. (e) Overview of number of droplets for respective cooling rates over time.

Nematic 5CB droplets

5CB is a thermotropic liquid crystal and a transition from the isotropic to the nematic phase is expected upon cooling. In the nematic phase, the liquid crystal exhibits a long-range orientational order without positional order. Volume confinement leads to an elastic distortion of the mesogen director field, typically resulting in topological defects, such as point defects with radial, bipolar or preradial configuration.[68,69] The type of mesogen arrangement in liquid crystal droplets is highly sensitive to their size, boundary conditions and/or external fields, which makes them ideally suited for biological and chemical sensing applications.

In the previous sections, the droplets remained in the isotropic phase. According to our recently published findings on the macroscopic behaviour of 5CB and MeOH and the corresponding phase diagram, the phase transition of MeOH-enriched 5CB from the isotropic to the nematic state is expected at −0.5 °C.[59] The controlled formation of nematic droplets was therefore subject of the following study. A homogeneous mixture of 5CB and MeOH was cooled from 35 °C to −5 °C, corresponding to a quench depth of 27.5 °C. Below the critical solution temperature, the droplets nucleated and grew by diffusion and coalescence. Fig. 5a and b shows bright-field images of droplets taken 2 seconds apart and reveal the isotropic-nematic transition, and the position of defects in the droplet. Fig. 5c shows polarised light micrographs of nematic 5CB droplets in MeOH that exhibit a radial configuration with homeotropic anchoring of the liquid crystal.

As shown in Fig. 5d, the diameter of the droplets increased rapidly when cooling through the isotropic temperature range. Upon reaching the nematic phase, the droplets remained stable in size over extended periods of time (here 45 min). The growth exponent of n = 0.36 was similar to the previously discussed isotropic quench (n = 0.35, ΔT = 7.5 °C). As shown in the ESI† (Fig. SI5), there is little motion of liquid crystal droplets and coalescence events were no longer observed. However, we found some evidence of Ostwald ripening; as some droplets increased

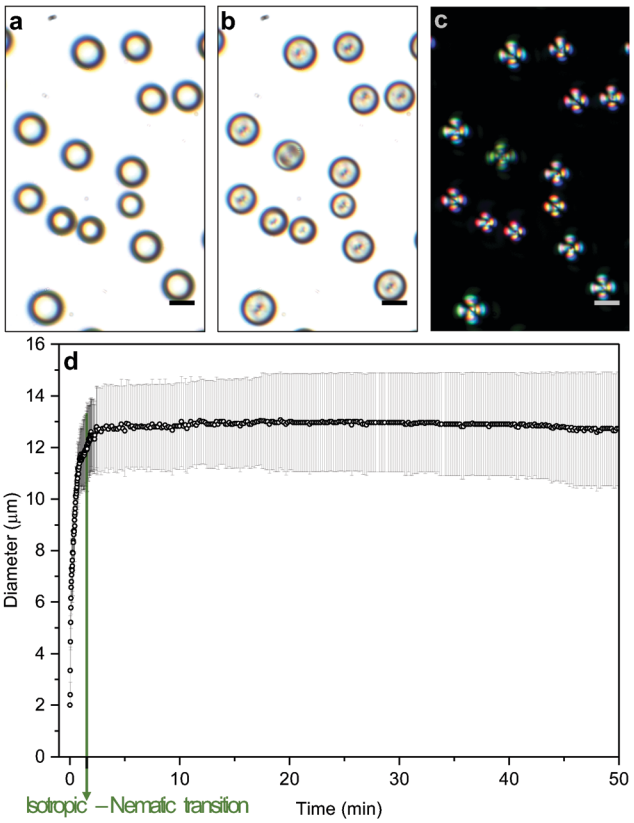

Fig. 5 Formation of nematic droplets. Image sequence for a temperature quench of 27.5 °C (a) Bright-field image of isotropic droplets just above the transition temperature. (b) Bright-field image of nematic droplets 2 seconds later. (c) Nematic droplets imaged under cross-polarised light. The scale bar represents 10 μm. (d) Overview of droplet mean diameter (with standard deviation) and temperature over time (Cooling rate: 20 °C min^{-1}).

in size, smaller droplets decreased in size and eventually diffused back into methanol.

Historically, nematic liquid crystal droplets have been prepared either through phase separation of a polymer – liquid crystal mixture (PDLC),[26] ultrasonic[70,71] or mechanical shearing[72] with optional fractionation.[73] or dispersion polymerization.[74] Recently, microfluidic preparation of LC droplets has become more widely used,[31,75,76] as well as a templating technique that relies on the sacrificial use of silica spheres and encapsulation by polyelectrolyte multilayers.[77,78] While conventional methods offer scalable solutions, their preparation is often plagued by a lack of size control. In contrast, microfluidic processing and polyelectrolyte multilayer templating offer access to well defined liquid crystal droplets, yet the former is limited to larger diameter and the latter involves a relatively elaborate preparative protocol. In comparison, the herein proposed route of nematic liquid crystal droplet formation distinguishes itself through the ease of fabrication and reversibility of formation.

Conclusion

In conclusion, we report on the controlled formation of liquid crystal microdroplets by a temperature-induced phase separation process and the identification of critical parameters that govern this phenomenon. The growth patterns were crucially dependent on the quench depth and the cooling rate of droplets. The temperature quench depth played a crucial role for the observed motion, affecting droplet size and dispersity. The cooling rate had a strong influence on the number of droplet nuclei. Upon cooling into the nematic regime, droplets adopted a radial configuration. Thus, phase segregation of liquid mixtures with a critical point of miscibility may offer control over nucleation and size evolution of droplets with ease of fabrication and reversibility of the process. Such transient LC droplets with well-defined size and mesogen arrangement provide a multitude of opportunities for materials templating and sensing applications. Further advances are in our view offered by the implementation in microfluidic platforms, which would allow for further improved spatial and temporal temperature control as well as droplet extraction.

Conflicts of interest

There are no conflicts to declare.

Acknowledgements

This project received funding from the European Union's Horizon 2020 research and innovation programme under grant agreement no. 633635 (DIACHEMO). MP acknowledges funding as part of the EPSRC Centre for Doctoral Training in Molecular Modelling and Materials Science (EP/L015862/1) in support of BASF SE.

Notes and references

1 C. Xu, H. Yu, S. Peng, Z. Lu, L. Lei, D. Lohse and X. Zhang, *Soft Matter*, 2017, **13**, 937–944.
2 F. Walton and K. Wynne, *Nat. Chem.*, 2018, **10**, 506–510.
3 J. M. Gunton, M. San Miguel and P. S. Sahni, in *Phase Transit. Crit. Phenom.*, ed. J. L. Lebowitz, Academic, London, 8th edn, 1983, p. 267.
4 J. W. Cahn and J. E. Hilliard, *J. Chem. Phys.*, 1959, **31**, 688–699.
5 J. W. Gibbs, *The Scientific Papers of J. Willard Gibbs*, Dover, New York, 1961, vol. 1.
6 A. J. Bray, *Phys. A*, 1993, **194**, 41–52.
7 H. Reiss and M. Shugard, *J. Chem. Phys.*, 1976, **65**, 5280.
8 J. Colombani and J. Bert, *J. Non-Equilib. Thermodyn.*, 2004, **29**, 389–395.
9 J. Feder, K. C. Russelt, J. Lothe and G. M. Pound, *Adv. Phys.*, 2006, **15**, 111–178.
10 J. J. D. Yoreo and P. G. Vekilov, *Rev. Mineral. Geochem.*, 2003, **54**, 57–93.
11 D. A. Porter and K. E. Easterling, *Phase Transformations in Metals and Alloys*, 1992, pp. 1–227.
12 K. Diekmann, M. Schumacher and H. Stegemeyer, *Liq. Cryst.*, 1998, **25**, 349–355.
13 I. Dierking, *J. Phys. Chem. B*, 2000, **104**, 10642–10646.

14 M. Rahimi, H. Ramezani-Dakhel, R. Zhang, A. Ramirez-Hernandez, N. L. Abbott and J. J. de Pablo, *Nat. Commun.*, 2017, **8**, 15064.
15 I. Lifshitz and V. V. Slyozov, *J. Phys. Chem. Solids*, 1961, **19**, 35–50.
16 A. J. Bray, *Phys. Rev. B: Condens. Matter Mater. Phys.*, 1990, **41**, 6724–6732.
17 I. Dierking, *Appl. Phys. A: Mater. Sci. Process.*, 2001, **72**, 307–310.
18 W. Mayer and D. Woermann, *J. Chem. Phys.*, 1990, **93**, 4349–4356.
19 M. Nakata and K. Kawate, *Phys. Rev. Lett.*, 1992, **68**, 2176–2179.
20 R. Mauri, F. Califano, E. Calvi, R. Gupta and R. Shinnar, *J. Chem. Phys.*, 2003, **118**, 8841–8846.
21 L. D. Zarzar, V. Sresht, E. M. Sletten, J. A. Kalow, D. Blankschtein and T. M. Swager, *Nature*, 2015, **518**, 520–524.
22 R. W. Style, T. Sai, N. Fanelli, M. Ijavi, K. Smith-Mannschott, Q. Xu, L. A. Wilen and E. R. Dufresne, *Phys. Rev. X*, 2017, **8**, 1–9.
23 S. Bronnikov and I. Dierking, *Phys. Chem. Chem. Phys.*, 2004, **6**, 1745–1749.
24 J. C. Loudet, P. Barois and P. Poulin, *Nature*, 2000, **507**, 611–613.
25 J. C. Loudet, *Liq. Cryst. Today*, 2005, **14**, 1–14.
26 H. G. Craighead, J. Cheng and S. Hackwood, *Appl. Phys. Lett.*, 1982, **40**, 22–24.
27 S. Bronnikov, S. Kostromin and V. Zuev, *J. Macromol. Sci., Part B: Phys.*, 2013, **52**, 1718–1735.
28 G. P. Crawford and S. Zumer, *Liquid Crystals In Complex Geometries: Formed by Polymer And Porous Networks*, CRC Press, 1996.
29 J. Gupta, J. S. Zimmerman, J. J. De Pablo, F. Caruso and N. Abbott, *Langmuir*, 2009, **25**, 9016–9024.
30 M. I. Kinsinger, M. E. Buck, N. L. Abbott and D. M. Lynn, *Langmuir*, 2010, **26**, 10234–10242.
31 W. Khan, J. H. Choi, G. M. Kim and S. Y. Park, *Lab Chip*, 2011, **11**, 3493–3498.
32 T. Lopez-Leon and A. Fernandez-Nieves, *Colloid Polym. Sci.*, 2011, **289**, 345–359.
33 A. Concellon, C. A. Zentner and T. M. Swager, *J. Am. Chem. Soc.*, 2019, **141**, 18246–18255.
34 Z. Li and Y. Yin, *Adv. Mater.*, 2019, **31**, 1807061.
35 W.-S. Wei, Y. Xia, S. Ettinger, S. Yang and A. G. Yodh, *Nature*, 2019, **576**, 433–436.
36 J. W. Doane, N. A. Vaz, B. G. Wu and S. Žumer, *Appl. Phys. Lett.*, 1986, **48**, 269–271.
37 P. S. Drzaic, *J. Appl. Phys.*, 1986, **60**, 2142–2148.
38 S. J. Woltman, G. D. Jay and G. P. Crawford, *Nat. Mater.*, 2007, **6**, 929–938.
39 V. J. Aliño, J. Pang and K. L. Yang, *Langmuir*, 2011, **27**, 11784–11789.
40 S. Sivakumar, K. L. Wark, J. K. Gupta, N. L. Abbott and F. Caruso, *Adv. Funct. Mater.*, 2009, **19**, 2260–2265.
41 I. Lin, D. S. Miller, P. J. Bertics, C. J. Murphy, J. J. D. Pablo and N. L. Abbott, *Science*, 2011, **332**, 1297–1300.
42 T. Bera and J. Fang, *Langmuir*, 2013, **29**, 387–392.
43 Y.-K. Kim, X. Wang, P. Mondkar, E. Bukusoglu and N. L. Abbott, *Nature*, 2018, **557**, 539–544.
44 M. Humar, M. Ravnik, S. Pajk and I. Muševič, *Nat. Photonics*, 2009, **3**, 595–600.
45 K. G. Noh and S. Y. Park, *Mater. Horiz.*, 2017, **4**, 633–640.
46 S. S. Lee, H. J. Seo, Y. H. Kim and S.-H. Kim, *Adv. Mater.*, 2017, **29**, 1606894.
47 M. Anyfantakis, V. S. R. Jampani, R. Kizhakidathazhath, B. P. Binks and J. P. F. Lagerwall, Angew. Chem., Int. Ed.
48 M. Humar and I. Muševič, *Opt. Express*, 2010, **18**, 26995.
49 S. S. Lee, J. B. Kim, Y. H. Kim and S.-H. Kim, *Sci. Adv.*, 2018, **4**, eaat8276.
50 L. Wang, D. Chen, K. G. Gutierrez-Cuevas, H. K. Bisoyi, J. Fan, R. S. Zola, G. Li, A. M. Urbas, T. J. Bunning, D. A. Weitz and Q. Li, *Mater. Horiz.*, 2017, **4**, 1190–1195.
51 P. Sleczkowski, Y. Zhou, S. Iamsaard, J. J. de Pablo, N. Katsonis and E. Lacaze, *Proc. Natl. Acad. Sci. U. S. A.*, 2018, **115**, 4334–4339.
52 J. Fan, Y. Li, H. K. Bisoyi, R. S. Zola, D. K. Yang, T. J. Bunning, D. A. Weitz and Q. Li, *Angew. Chem., Int. Ed.*, 2015, **54**, 2160–2164.
53 C. C. Maass, C. Krueger, S. Herminghaus and C. Bahr, in *Annual Review Of Condensed Matter Physics*, ed. M. C. Marchetti and S. Sachdev, 2016, pp. 171–193, vol. 7 of Annual Review of Condensed Matter Physics.
54 C. Krueger, G. Kloes, C. Bahr and C. C. Maass, *Phys. Rev. Lett.*, 2016, **117**, 048003.
55 C. Jin, C. Krüger and C. C. Maass, *Proc. Natl. Acad. Sci. U. S. A.*, 2016, **114**, 5089–5094.
56 X. Wang, E. Bukusoglu and N. L. Abbott, *Chem. Mater.*, 2017, **29**, 53–61.
57 A. N. Radhakrishnan, M. P. Marques, M. J. Davies, B. O'Sullivan, D. G. Bracewell and N. Szita, *Lab Chip*, 2018, **18**, 585–594.
58 I. F. Sbalzarini and P. Koumoutsakos, *J. Struct. Biol.*, 2005, **151**, 182–195.
59 L. A. Serrano, M. J. Fornerod, Y. Yang, F. Stellacci and S. Guldin, *Soft Matter*, 2018, **14**, 4615–4620.
60 M. J. Fornerod, E. Amstad and S. Guldin, *Mol. Syst. Des. Eng.*, 2020, **5**, 358–365.
61 C. G. Reyes, J. Baller, T. Araki and J. P. F. Lagerwall, *Soft Matter*, 2019, **15**, 6044–6054.
62 S. Buil, J. P. Delville and A. Ducasse, *Phys. Rev. Lett.*, 1999, **82**, 1895–1898.
63 S. Luo, J. Schiffbauer and T. Luo, *Phys. Chem. Chem. Phys.*, 2017, **19**, 29855–29861.
64 A. C. Pan, T. J. Rappl, D. Chandler and N. P. Balsara, *J. Phys. Chem. B*, 2006, **110**, 3692–3696.
65 H. Tanaka, *Phys. Rev. Lett.*, 1994, **72**, 1702–1705.
66 H. Tanaka, *J. Chem. Phys.*, 1996, **105**, 10099–10114.
67 D. S. Martula, R. T. Bonnecaze and D. R. Lloyd, *Int. J. Multiphase Flow*, 2003, **29**, 1265–1282.
68 T. Lopez-Leon and A. Fernandez-Nieves, *Phys. Rev. E: Stat., Nonlinear, Soft Matter Phys.*, 2009, **79**, 1–5.
69 E. Pairam, J. Vallamkondu, V. Koning, B. C. Van Zuiden, P. W. Ellis, M. A. Bates, V. Vitelli and A. Fernandez-Nieves, *Proc. Natl. Acad. Sci. U. S. A.*, 2013, **110**, 9295–9300.
70 T. Tixier, M. Heppenstall-Butler and E. M. Terentjev, *Langmuir*, 2006, **22**, 2365–2370.
71 D. S. Miller and N. L. Abbott, *Soft Matter*, 2013, **9**, 374–382.

72 F. Mondiot, X. Wang, J. J. De Pablo and N. L. Abbott, *J. Am. Chem. Soc.*, 2013, **135**, 9972–9975.
73 P. Hsu, P. Poulin and D. A. Weitz, *J. Colloid Interface Sci.*, 1998, **200**, 182–184.
74 M. Vennes and R. Zentel, *Macromol. Chem. Phys.*, 2004, **205**, 2303–2311.
75 A. Fernández-Nieves, G. Cristobal, V. Garcés-Chávez, G. C. Spalding, K. Dholakia and D. A. Weitz, *Adv. Mater.*, 2005, **17**, 680–684.
76 M. Urbanski, C. G. Reyes, J. Noh, A. Sharma, Y. Geng, V. Subba Rao Jampani and J. P. Lagerwall, *J. Phys.: Condens. Matter*, 2017, **29**, 133003.
77 N. Abbott, S. Sivakumar, J. Gupta and F. Caruso, *Chem. Mater.*, 2008, **20**, 7743–7745.
78 J. K. Gupta, S. Sivakumar, F. Caruso and N. L. Abbott, *Angew. Chem., Int. Ed.*, 2009, **48**, 1652–1655.
79 A. Karbalaei, R. Kumar and H. J. Cho, *Micromachines*, 2016, **7**, 13.